


 Cite this: *RSC Adv.*, 2024, **14**, 4165

Exploring the mechanical, vibrational optoelectronic, and thermoelectric properties of novel half-Heusler FeTaX (X = P, As): a first-principles study

 Tesfaye Abebe Geleta,^{ab} D. Behera,^c Ramesh Sharma,^{ab} Murefah mana Al-Anazy,^d El Sayed Yousef,^{ef} Vipul Srivastava^{gh} and A. J. A. Moayad^{hi}

In this study, the density functional theory (DFT) was employed to study the structural, electronic, optical, and thermoelectric characteristics of half-Heusler (HH) FeTaX (X = P or As). Optimization of the structures was achieved using Perdew–Burke–Ernzerhof (PBE) parametrized generalized gradient approximation (GGA). These HH FeTaX (X = P, As) showed indirect bandgaps of 0.882 eV and 0.748 eV, respectively. The predicted density of states (DOS) spectra suggest that Fe-d and Ta-d states contribute predominantly to both valence and conduction bands, whereas P/As-p states contribute less. Optical properties were investigated to assess their potential in optoelectronic applications. The estimated values of various optical parameters and low loss suggest that the studied HH FeTaX (X = P, As) are suitable for optoelectronic device applications. The thermoelectric responses of the studied HH FeTaX (X = P, As) were computed, and their highest power factors at high temperature reflects their usage in thermoelectric devices.

 Received 6th December 2023
 Accepted 6th January 2024

DOI: 10.1039/d3ra08317a

rsc.li/rsc-advances

1. Introduction

In response to the escalating energy demands and the depletion of natural resources, there is a pressing necessity for alternative energy sources. A promising approach to address this issue is the development of novel thermoelectric (TE) materials that enable the direct conversion of waste heat into electricity.^{1–3} The performance of these materials in thermoelectric devices can be assessed using a parameter known as the figure of merit (*ZT*). *ZT* is expressed as $S^2\sigma T/\kappa$, where $S^2\sigma$ stands for the power factor

(PF), S is the Seebeck coefficient, σ is the electrical conductivity, κ is the thermal conductivity, and T is the absolute temperature. For maximum performance, a material must have low κ and optimum $S^2\sigma$.^{4,5} Owing to their outstanding mechanical stability and high *ZT* values, half-Heusler materials are currently attracting the attention of researchers.

HH materials that are examined so far are bulk TE materials, which largely fulfill these criteria. HH materials are well-suited for various applications, including large-scale TE power generation as well as magnetic and spintronic applications. Although their high thermal conductivity in a lattice restricts their overall efficiency in converting heat to electricity, their strong electrical properties make them suitable for power generation applications.^{6–8} Owing to their excellent combination of technical attributes and TE performances, HH materials stand out as promising candidate for TE applications.

Therefore, the focus of several theoretical and experimental investigations is their transport features. Materials with an 8-valence electron count are predicted to have a semiconducting nature. Based on the atoms that make up their structure, HH compounds (those with 8 valence electrons) may have a broad bandgap. For instance, 20 HH compounds, according to Thomas Gruhn *et al.*, are suitable for optical purposes.⁹ P. S. Kacimi *et al.* studied I-II-V and I-III-IV HH compounds, revealing their physical properties.¹⁰ The thermoelectricity of KScM (M = C and Ge) HH materials, which exhibit considerable transport qualities, have been reported by Yasemin O. Ciftci

^aGraduate Institute of Applied Science and Technology, National Taiwan University of Science and Technology, Taipei 10607, Taiwan

^bMacDermid Alpha Electronics Solutions Company, Taoyuan 32062, Taiwan

^cDepartment of Applied Science, Feroze Gandhi Institute of Engineering and Technology, Raebareli, Uttar Pradesh, India. E-mail: sharmadft@gmail.com

^dDepartment of Chemistry, College of Sciences, Princess Nourah bint Abdulrahman University (PNU), P. O. Box 84428, 11671, Riyadh, Saudi Arabia

^eResearch Center for Advanced Materials Science (RCAMS), King Khalid University, P. O. Box 9004, Abha 61413, Saudi Arabia

^fDepartment of Physics, Faculty of Science, King Khalid University, P. O. Box 9004, Abha, Saudi Arabia

^gDepartment of Physics, School of Chemical Engineering and Physical Sciences, Lovely Professional University, Phagwara, Punjab 144411, India. E-mail: vipsri27@gmail.com

^hDepartment of Research Impact & Outcome, Research & Development Cell, Lovely Professional University, Phagwara, Punjab 144411, India

ⁱDepartment of Materials Science, Malawi University of Science and Technology, P. O. Box 5196, Limbe, Malawi. E-mail: mailme_moya123@rediffmail.com



*et al.*¹¹ In their study, they found that its thermoelectricity was 1.5 times greater than Bi_2Te_3 . Half-Heusler compounds have great thermal stability, outstanding electrical characteristics, and excellent mechanical resilience, which make them potential mid-to-high-temperature thermoelectric materials. Other factors to consider while using these HH compounds in thermoelectric applications include their availability and high value of power factor. Ciesielski *et al.* investigated the high-temperature power factor of HH RENiSb (RE = Sc, Dy, Ho, Er, Tm, Lu).¹² Winiarski *et al.* studied the thermoelectric behaviour of the p-type half-Heusler alloy ScMSb (M = Ni, Pd, Pt) using *ab initio* calculations.¹³ Pan *et al.* investigated superconductivity and magnetic order in the non-centrosymmetric half-Heusler compound ErPdBi.¹⁴ Furthermore, traditional techniques have substantially reduced the typically high lattice thermal conductivity of conventional ternary half-Heusler compounds, such as ZrNiSn, TiCoSb, and NbFeSb. For example, using band engineering or multi-element alloying, ZT values of more than 1.3 were obtained for n-type materials, such as (Ti, Zr, Hf) NiSn.¹⁵ The wide range of HH compositions makes it simpler to find, alter, or produce materials suitable for TE and spintronic applications. Recently, the use of nanocomposites, nanostructuring, and isoelectronic alloying has improved the TE efficiency of HH semiconductors.^{16,17} This improvement, however, significantly depends on the high ZT values of the optimal parent alloys. Advancements have been made to increase the TE efficiency of HH semiconductors by employing nanocomposites, nanostructuring, and isoelectronic alloying.⁸⁻¹⁸ This progress, however, primarily relies on the excellent ZT values of the parent alloys.

Wang *et al.*¹⁹ experimentally demonstrated an enhancement in the thermoelectric performance of Ti(Fe, Co, Ni)Sb half-Heusler alloys by varying the ratio of Fe/Co/Ni. They could achieve power factors as high as $1.80 \text{ mW m}^{-1} \text{ K}^{-2}$ and $2.21 \text{ mW m}^{-1} \text{ K}^{-2}$ and ZT values 0.65 and 0.85 at 973 K for n-type $\text{TiFe}_{0.3}\text{Co}_{0.2}\text{Ni}_{0.5}\text{Sb}$ and p-type $\text{TiFe}_{0.5}\text{Co}_{0.15}\text{Ni}_{0.35}\text{Sb}$, respectively. Attempts have been made to reduce the lattice thermal conductivity of half-Heusler compounds, including TiCoSb, ZrNiSn and NbFeSb. Multi-element alloying has been shown to obtain high ZT values (~ 1.2) in the half-Heusler compounds (Ti, Zr, Hf)NiSn, with low lattice thermal conductivity $\sim 2 \text{ W m}^{-1} \text{ K}^{-1}$. Among the compounds found by Zhu *et al.*,²⁰ the p-type TaFeSb-based half-Heusler material showed very promising thermoelectric performance. It achieved a ZT peak of approximately 1.52 at 973 K and an average ZT of around 0.93 in the 300–973 K temperature range. However, when the structural, elastic, mechanical, electronic, magnetic and optical properties of half-Heusler compounds CoFeZ (Z = P, As, Sb) were investigated by Zahir *et al.*²¹ using GGA + U approximation, these materials were found to be optically active in the range of intermediate energy. *i.e.* between (2–30) eV.

These established facts and studies on different materials motivated us to explore a new group of HH compounds, namely FeTaX (X = P, As). These materials are of great importance due to anomalous characteristics with respect to their semiconducting nature, low energy band gap, good optical conductivity, moderate PF, and thermal and electrical conductivities.

In this work, we have utilized first-principles calculations based on DFT in combination with the semiclassical Boltzmann theory. Specifically, our study focuses on examining physical characteristics, including mechanical, vibrational optoelectronic and thermoelectric properties, of FeTaX (X = P, As) HH materials. To our knowledge, these compounds have not been thoroughly examined in the past. In this research, we have employed the hypothetical Tran-Blaha-modified Becke-Johnson exchange (Tb-mBJ)²² to precisely compute bandgap. Our findings show that the FeTaX (X = P, As) HH compounds may be suitable for thermoelectric generators and optical devices.

2. Computational method

The computations in this work were aimed at quantum mechanics and carried out considering the WIEN2k code²³ in DFT based on the linearized augmented plane wave (FP-LAPW) technique.²⁴ The electronic exchange-correlation energy (GGA-PBE)²⁵ was employed for analyzing the structural features using generalized gradient approximation based on Perdew *et al.* A $R_{\text{MT}} \times K_{\text{MAX}}$ cut-off value of 7.0 was used in this study.²⁶ K_{MAX} denotes the reciprocal lattice vectors with the largest selected value to expand the plane wave. RMT is the smallest atomic radius. A self-consistent accuracy of total energy = 10^{-4} Ry was employed in the simulations. The radii of the Fe, Ta, P, and As atoms in the MT atomic spheres (R_{MT}) were taken as 2.01, 1.96, 2.35, and 2.45 au, respectively. The energy concentration was set up to 10^{-6} Ry. The elastic properties were computed using the IRelast software package.²⁷

Optical investigations are commonly employed to determine the electronic band structure of solids in a quantitative manner. In this regard, the optical performance of the considered materials was examined using the WIEN2K code.

The dielectric function $\varepsilon(\omega)$ provides valuable insights into the optical properties of a material as it quantifies the linear response of the system to an external electromagnetic field and is described by the equation formulated by Ehrenreich and Cohen,²⁸ as shown below.

$$\varepsilon(\omega) = \varepsilon_1(\omega) + i\varepsilon_2(\omega). \quad (1)$$

The formula for the imaginary part $\varepsilon_2(\omega)$ is

$$\varepsilon_2(\omega) = \frac{\omega_p^2}{8\pi^3 c^3 \tau} \lambda^3 \quad (2)$$

Moreover, Kramers–Kronig Transformation (KKT) gives the value of the real part of $\varepsilon(\omega)$ *i.e.* $\varepsilon_1(\omega)$

$$\varepsilon_1(\omega) = 1 + \frac{2}{\pi} M \int_0^\infty \frac{\omega' \varepsilon_2(\omega')}{\omega'^2 - \omega^2} d\omega' \quad (3)$$

We also calculated the refractive index $n(\omega)$ based on the complex dielectric function, as follows:²⁹

$$n(\omega) = \frac{1}{\sqrt{2}} \left(\varepsilon_1 + (\varepsilon_1^2 + \varepsilon_2^2)^{1/2} \right)^{1/2} \quad (4)$$



The reflectivity $R(\omega)$ was obtained directly from $\varepsilon_1(\omega)$ and $\varepsilon_2(\omega)$.

Further, the BoltzTrap code³⁰ using the semi-classical Boltzmann theory was used to examine the thermoelectric properties. The thermoelectric parameters, including figure of merit (ZT), power factor (PF), and electrical and thermal conductivities, were evaluated. A material that has $ZT \sim 1$ is efficient for thermoelectric generators; however, its applicability further depends on various parameters, such as PF and thermal conductivity (κ/τ), where τ ($\sim 10^{-15}$) is the relaxation time.

$$ZT = \text{PF}/(\kappa/\tau)T \quad (5)$$

where PF further depends on the Seebeck coefficient (S) and electrical conductivity (σ/τ).

$$\text{PF} = S^2 \sigma/\tau \quad (6)$$

where the Seebeck coefficient (S) measures the magnitude of the thermoelectric voltage induced between two materials when a particular temperature difference is maintained between them.

3. Results and discussion

3.1. Structural properties

As shown in Fig. 1, we estimated the optimized structure of the investigated HH FeTaX (X = P, As) and found that they exist as cubic

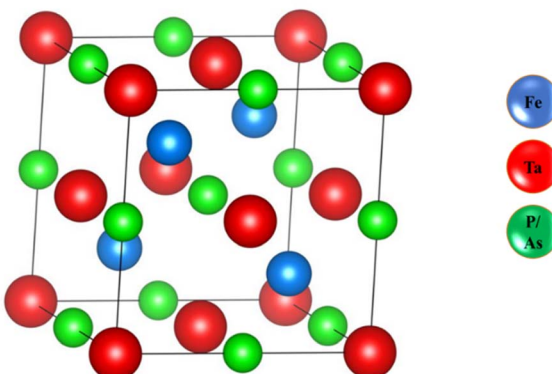


Fig. 1 The optimized structure of the FeTaX (X = P, As) compounds. The blue balls represent Fe atoms, the red balls represent Ta atoms, and the green balls represent P or As atoms.

Table 1 The calculated lattice parameter (a), unit cell volume (V), bulk modulus (B), first order pressure derivative of B (B'), optimized total energy (E_{Total}), formation energy (E_{Form}), and Bader charge of FeTaX (for X = P, As). The parameters were calculated for configurations in magnetic and non-magnetic phases. (Bader charge: "+" denotes addition of electrons, "-" denotes removal of electrons)

HHs	a (Å)	V (au) ³	B (GPa)	B' (Gpa)	E_{Total} (Ry)	E_{Form} (eV per atom)	Bader charges
FeTaP	5.58	293.17	233.16	6.31	-34482.164127	-0.45	Fe = 0.98 P = 0.78 Ta = -0.72
FeTaAs	5.72	316.70	202.57	4.85	-38320.084029	-0.49	Fe = 0.96 As = 0.74 Ta = -0.68
Other works	5.86 [theory] ³⁴ 5.89 [expt] ^{19,61}		195.59 [theory] ³⁴	4.17 [theory] ³⁴	—	—	—



crystal structures (SG: $Fm\bar{3}m$). The Fe, Ta, and X atoms are positioned at 2a (0, 0), 2d (1/3, 2/3, 3/4), and 2c (1/3, 2/3, 1/4), respectively. Table 1 shows computed values of the structural parameters. Furthermore, to assess the structural stability, we computed the lattice parameters based on the Birch–Murnaghan equation,³¹ as shown in Fig. 2. Table 1 compares results from past investigations with the estimated lattice constant and unit cell volume of FeTaX (X = P, As). The computed outcomes are in accordance with other experimental and theoretical reports.^{19,34} Furthermore, we computed the formation energy (E_{form}) to evaluate the thermodynamical stability of the considered materials using eqn (7):

$$E_{\text{form}} = E_{\text{Total}}^{\text{FeTaX}} - E_{\text{Fe}}^{\text{bulk}} - E_{\text{Ta}}^{\text{bulk}} - E_{\text{X}}^{\text{bulk}} \quad (7)$$

The computed formation energies for FeTaP and FeTaAs were -0.45 eV per atom and -0.59 eV per atom, respectively, indicating the stability of these compounds.³² The negative formation energy values confirm their stability. In order to determine their dynamic stability, we computed phonon dispersion using the Vienna *Ab initio* Simulation Package (VASP). The phonon dispersion plots of FeTaX (X = P, As) are represented in Fig. 3. The absence of imaginary frequencies in the plots represents the dynamic stability of the investigated compounds.

3.2. Elastic properties

While designing solids for commercial applications, it is crucial to consider their mechanical properties, such as anisotropy (A), bulk modulus (B), shear modulus (G), Pung ratio (B/G), and second-order elastic constants (C_{ij} for $i, j = 1, 2$). In a cubic system, the dimensional strength relies on the interplay of three elastic constants: C_{11} representing resistance to strain, C_{12} signifying shear stress, and C_{44} indicating opposition to shear deformation.³³ Table 2 provides the calculated elastic constants for the cubic FeTaX (X = P, As) compounds in comparison with other theoretical and experimental results³⁴ and demonstrates good agreement with them. To assess the stability of the combinations under investigation, the Born–Huang stability condition^{35,36} was applied, as stated below:

$$(C_{11} - C_{12})/2 > 0, (C_{11} + 2C_{12}) > 0, C_{44} > 0 \quad (8)$$

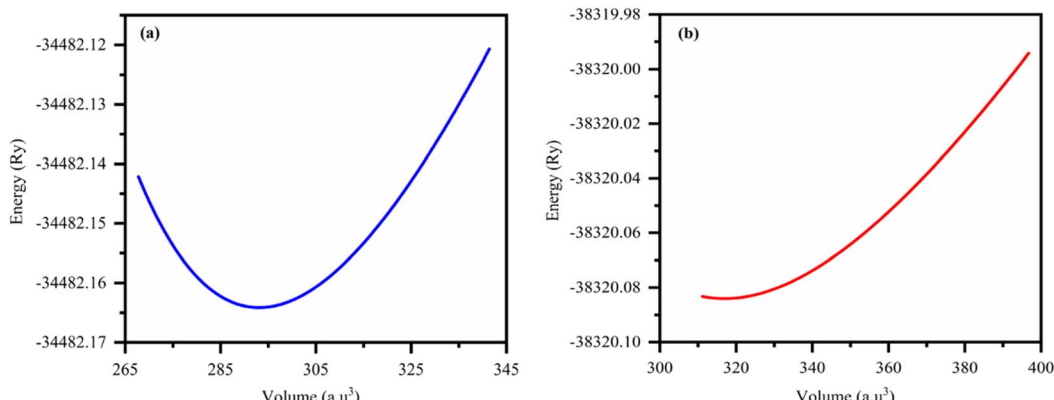


Fig. 2 The total energy versus volume optimization curves for (a) FeTaP and (b) FeTaAs.

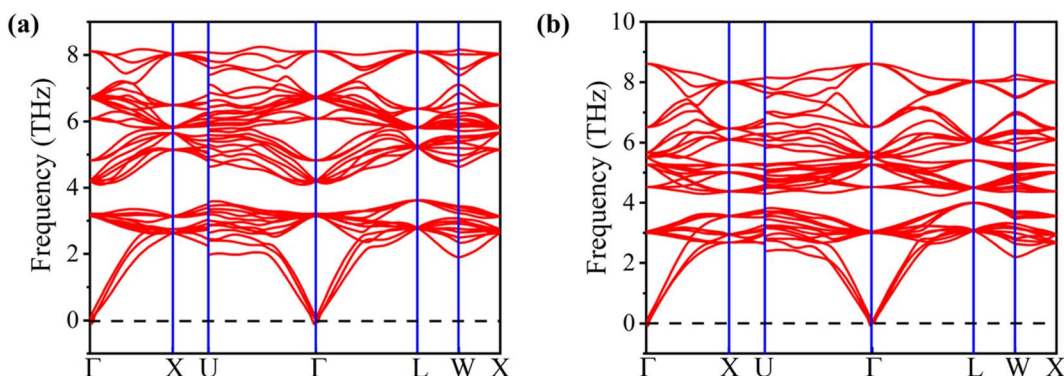


Fig. 3 The phonon dispersion plots for (a) FeTaP and (b) FeTaAs HHS.

The compounds can be considered stable based on our computational assessment as they fulfill the Born–Huang stability criteria. We used the following equations to calculate a range of elastic constants, namely bulk modulus (B), shear modulus (G), Young's modulus (Y), Poisson's ratio (ν), and anisotropy (A), with a focus on cubic structures.

$$B = \frac{C_{11} + 2C_{12}}{3} \quad (9)$$

$$G = \frac{C_{11} - C_{12}}{2} \quad (10)$$

$$Y = \frac{9GB}{3B + G} \quad (11)$$

$$\nu = \frac{3B - 2G}{2(3B + G)} \quad (12)$$

$$A = \frac{2C_{44}}{C_{11} - C_{12}} \quad (13)$$

The bulk modulus (B) of a material indicates its resistance to volume change when subjected to compression and reflects its crystal strength. A higher B value signifies greater crystal strength. On the other hand, the shear modulus (G) quantifies

the ability of the crystal to resist plastic deformation. In the case of the FeTaX ($X = P, As$) compounds, the estimated B values were 96.37 GPa and 120.5 GPa, respectively.³⁷ This suggests that FeTaAs exhibits greater resistance to volume change than FeTaP due to its higher B value. Additionally, the higher G value of FeTaAs indicates stronger resistance to transverse bending. Pugh ratio (B/G) is the measure of brittleness or ductility of a material.^{38,39} If the B/G ratio exceeds 1.75, the material is considered ductile; otherwise, it is considered brittle. Table 2 provides the estimated B/G values of the FeTaX ($X = P, As$) compounds, indicating their inherent ductility. Frantsevich *et al.* used the Poisson ratio (ν) to distinguish between brittleness and ductility, with 0.26 serving as the critical value for these characteristics. When ν falls below 0.26, the material is considered brittle; when it exceeds 0.26, it is considered ductile.⁴⁰ The estimated values of the FeTaX ($X = P, As$) compounds were 0.27 and 0.26, respectively, affirming their ductile nature. This assessment was further corroborated by Cauchy pressure calculation based on the formula $C_p = C_{12} - C_{44}$. The positive Cauchy pressure values obtained for the examined compounds indicate the ionic nature of their crystal bonds.⁴¹ Moreover, $A = 1$ suggests isotropic crystals, while values other than 1 indicate anisotropy.^{42,43} Two thermodynamic factors related to elastic properties, namely melting point (T_m) and Debye temperature (θ_D), were also investigated. The



Table 2 The calculated values of the elastic constants C_{11} , C_{12} , C_{44} ; bulk modulus B ; shear modulus G (GPa); Young's modulus E ; bulk modulus to shear modulus ratio B/G ratio; Poisson's ratio ν ; Zener anisotropy factor A ; Cauchy pressure C_p ; sound velocity (transverse v_t ; longitudinal v_l ; mean v_m); Debye temperature θ_D ; and melting temperature T_m of the FeTaX (for $X = P, As$) compounds using PBE-GGA

Parameters	Other works		Other works	
	FeTaP	FeTaAs	Theory ³⁴	Expt ⁶²
C_{11} (GPa)	175.31	209.3	304.82	184.7, 214.9
C_{12} (GPa)	56.90	76.2	156.93	
C_{44} (GPa)	51.34	69.4	117.97	
B (GPa)	96.37	120.5	206	
G (GPa)	54.57	70.1	97.82	
E (GPa)	137.61	174.4		161.1, 171.6
B/G (GPa)	1.77	1.79	2.11	
ν	0.27	0.26	0.295	
A (GPa)	0.85	1.07		0.223, 0.271
$C_p = (C_{12} - C_{44})$ (GPa)	4.66	6.8		
v_t (m s ⁻¹)	2524	3266		
v_l (m s ⁻¹)	4341	5631		
v_m (m s ⁻¹)	2801	3621		
θ_D (K)	307.5	407.3		
T_m (K)	2912.3	3461		

Debye temperature (θ_D) was determined based on the mean sound velocity (v_m) using the formula:⁴⁴

The calculated Debye temperature values are presented in Table 2. The mean sound velocity (v_m) in the substances under investigation was determined using the equation:

$$v_m = \left[\frac{1}{3} \left(\frac{2}{v_l^3} + \frac{1}{v_t^3} \right) \right]^{(1/3)} \quad (14)$$

where the longitudinal (v_l) and transverse (v_t) sound velocities are derived from the shear modulus and bulk modulus, respectively, as given below.

$$v_t = \sqrt{\frac{G}{\rho}} \text{ and } v_l = \sqrt{\frac{3B + 4G}{3\rho}} \quad (15)$$

Table 2 presents the calculated values of v_t , v_l , v_m , θ_D , and T_m

3.3. Electronic properties

The electronic properties computed for FeTaX (X = P, As) are represented in Fig. 4. The GGA-PBE functional generally underestimates bandgap values, while multiple investigations have demonstrated that the TB-mBJ potential may predict bandgap values that are closer to the experimental values. The illustrations demonstrate that the valence band (VB) maximum is at the L-point, and the conduction band (CB) minimum is at the X-point in the first Brillouin zone for both compounds.⁴⁵ These results suggest that FeTaP and FeTaAs are indirect band gap semiconductors with computed bandgaps of about 0.882 eV and 0.748 eV, respectively, by employing the GGA functional, as depicted in Fig. 4(a) and (d). Additionally, the bandgaps of FeTaP and FeTaAs computed using the TB-mBJ functional were enhanced, reaching 0.916 eV and 1.002 eV, respectively, as demonstrated in Fig. 4(b) and (e). Moreover, when spin-orbit coupling (SOC) was included, the band gap values reduced to

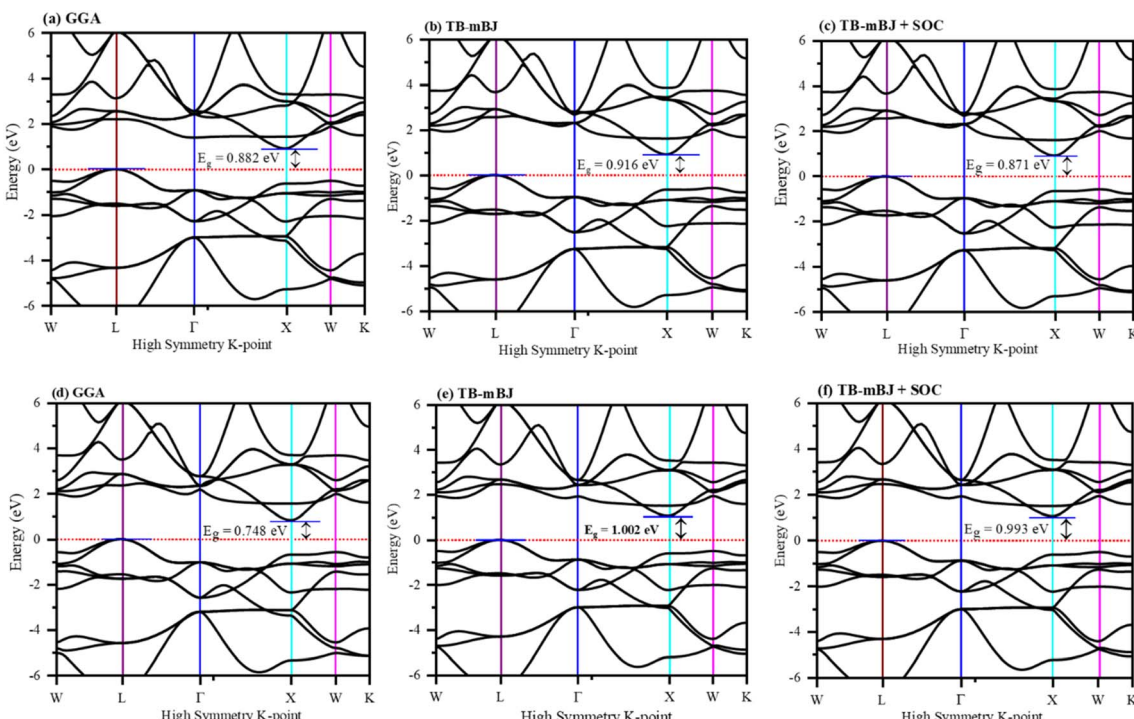


Fig. 4 The band structure of (a)–(c) FeTaP and (d)–(f) FeTaAs evaluated using (a) and (d) GGA, (b) and (e) TB-mBJ, and (c) and (f) TB-mBJ + SOC. The Fermi level is set to zero.



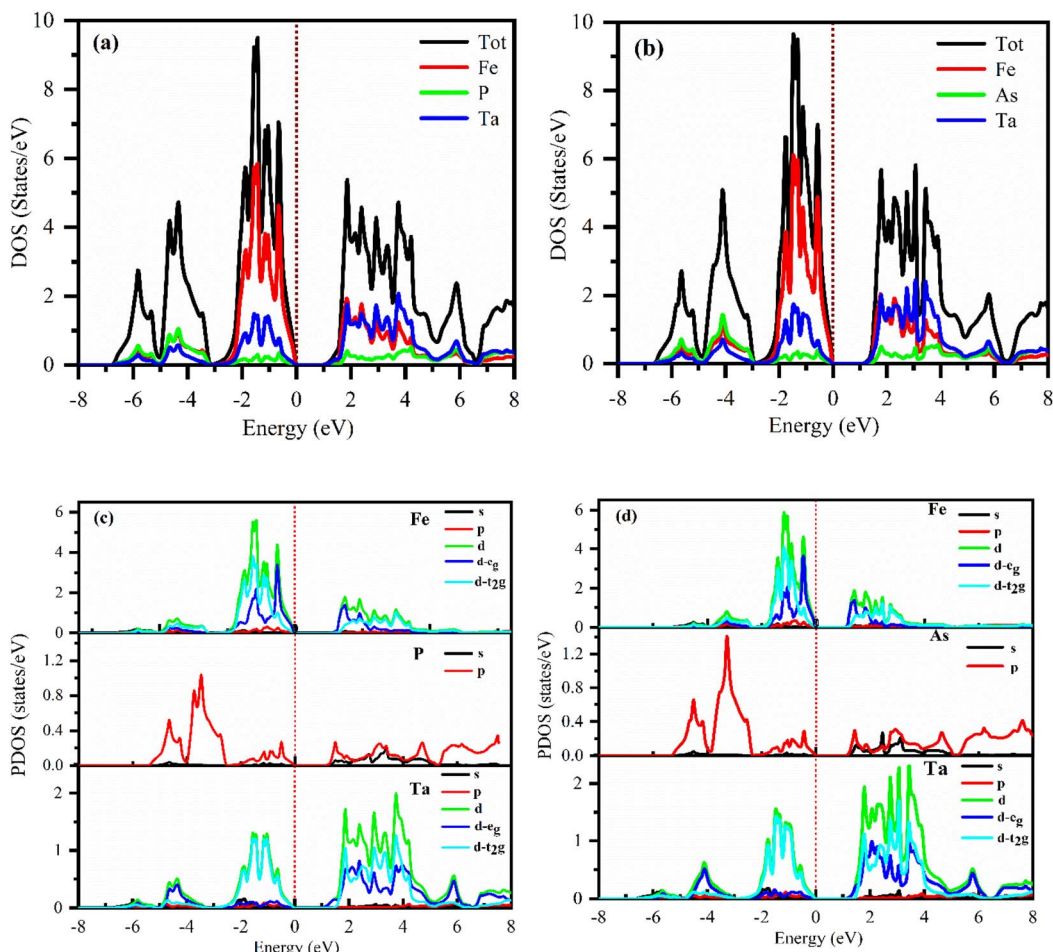


Fig. 5 DFT-calculated total DOS (a) and (b) and (c) and (d) partial DOS of (a) and (c) FeTaP and (b) and (d) FeTaAs. The Fermi level is set at zero.

0.871 eV and 0.993 eV for FeTaP, and FeTaAs, respectively, as shown in Fig. 4(c) and (f). Degeneration of the CB maximum at the X-point of FeTaX increased due to SOC, with splitting between the states respectively, confirming a strong SOC effect on the band structure feature of the FeTaX (X = P and As) compounds.⁴⁶ However, the maximum bandgap was obtained from the mBJ compared with mBJ + SOC. Therefore, we considered mBJ for further computations. The density of states

(DOS) helps us understand how different atomic states affect the band structure. Therefore, in Fig. 5, total and partial DOS obtained using the TB-mBJ functional are presented. Fig. 5(a) and (b) clearly signify that the VB is dominated by the Fe-d state, and the CB is mainly dominated by a combination of the Fe/Ta-d states with approximately equal intensities in both compounds.^{47,48} Furthermore, the lower intensity of the peaks associated with the P and As atoms in both compounds

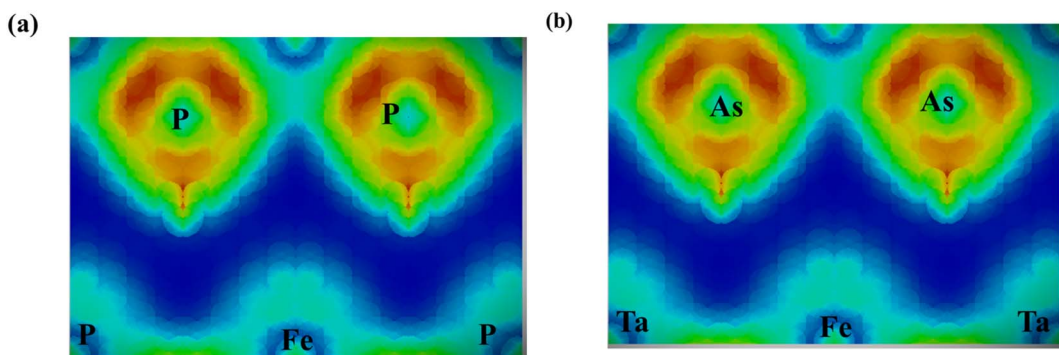


Fig. 6 Electron density plots for (a) FeTaP and (b) FeTaAs.

indicates that the presence of these atoms has a minimal impact on the VB and CB. Furthermore, the PDOS demonstrated in Fig. 5(c) and (d) shows the contribution of individual atoms to the VB and CB. In general, the bandgap increases with the substitution of atoms with larger ionic radii, such as As instead of P. This is due to the fact that the ionic radius increases as one moves down the periodic table.

We also calculated the effective mass of electrons and holes using the following relationship:

$$\frac{1}{m^*} = \frac{1}{\hbar^2} \frac{d^2 E_n(k)}{dk^2} \quad (16)$$

Accordingly, the effective masses of electrons and holes in FeTaX (X = P and As), respectively, were around 0.35 and 0.13 (FeTaP) and 0.36 and 0.17 (FeTaAs). The results indicate that the HHs under investigation exhibit extremely low effective carrier masses.⁴⁹ This reduced effective mass is advantageous for solar materials as it facilitates efficient carrier mobility. According to these findings, FeTaX (where X can be P or As) can demonstrate effectiveness in photovoltaic applications. To investigate the bonding between the constituent atoms, we analyzed the electronic density of those atoms. The blue contours represent electron loss, while the red counters represent electron gain in

Fig. 6. As shown in Fig. 6(a) and (b), the As atom accepts electrons from the Fe-Ta network. This is additionally confirmed by the negative Bader charge of 'As', as presented in Table 1, which supports the aforementioned outcomes.

3.4. Optical properties

We estimated the optical properties of FeTaX (X = P, As) in response to electromagnetic radiation. The TB-mBJ functional was used to calculate all the parameters. Fig. 7 shows the predicted optical characteristics of FeTaX (X = P, As) for up to 10 eV. The complex dielectric function $\varepsilon(\omega)$ was employed to determine the optical response of the studied compounds. Fig. 7(a) displays the computed real dielectric function $\varepsilon_1(\omega)$ versus photon energy. At zero energy level, it is known as static dielectric constant $\varepsilon_1(0)$, which was found to be 19.66 and 19.96 for FeTaP and FeTaAs, respectively. The variation in the magnitude of $\varepsilon_1(\omega)$ is closely associated with the bandgap.⁵⁰ The value was observed to increase and attained the maximum value at 1.98 eV and 1.96 eV, respectively, for FeTaP and FeTaAs; then, they decreased drastically to zero at about 4.1 eV and 3.8 eV, respectively. The variation in the $\varepsilon_2(\omega)$ spectra of the FeTaX (X = P, As) compounds with respect to photon energy is represented in Fig. 7(b), which is characterized by two main peaks (marked

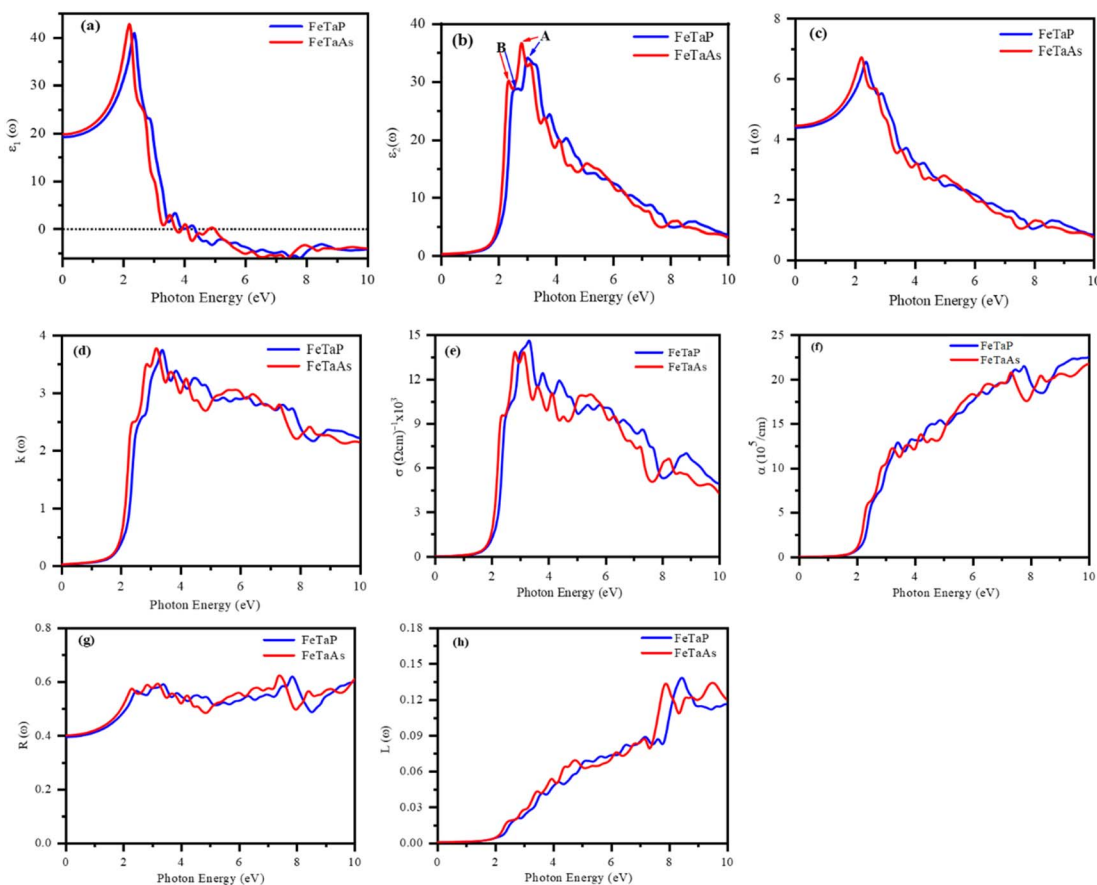


Fig. 7 DFT-calculated optical spectra of the (a) real component $\varepsilon_1(\omega)$ and (b) imaginary component $\varepsilon_2(\omega)$ of the dielectric function, (c) refractive index $n(\omega)$, (d) extinction coefficient $k(\omega)$, (e) optical conductivity $\sigma(\omega)$, (f) absorption coefficient $\alpha(\omega)$, (g) optical reflectivity $R(\omega)$, and (h) energy loss $L(\omega)$ of FeTaX (X = P, As).



as A and B) in the visible region. Both first peaks (A) of $\varepsilon_2(\omega)$ at 2.78/3.00 eV are principally due to the transition from the Fe d-d states, while the second B peaks at 2.35/2.62 eV originate from the Ta d-d state transition.

Fig. 7(c) shows the variation in refractive index $n(\omega)$ as a function of photon energy. Refractive index $n(0)$ showed static values of 4.43 and 4.46 for FeTaP and FeTaAs, respectively. These $n(0)$ values fulfill the relationship $n(0)^2 = \varepsilon_1(0)$,⁵¹ validating the calculation precision. We found that $n(\omega)$ in the infrared region reached the highest magnitude at 2.1/2.12 eV for FeTaP/As, then started falling and finally reached unity after 8 eV photon energy. The significant decrease in $n(\omega)$ within the visible region strongly indicates that the suggested materials are valuable candidates for future optical device applications.

The amount of light lost into the medium as a result of absorption and scattering per unit volume is known as the extinction coefficient $k(\omega)$.⁵² Fig. 7(d) displays the variation in extinction coefficient with photon energy. The first high peak of the extinction coefficient represents the photon energy. For the compounds FeTaP and FeTaAs, this was centered at 1.98 eV and 1.96 eV, respectively, corresponding to zero of $\varepsilon_2(\omega)$.

When an object is exposed to electromagnetic radiation, the covalent bonds are disrupted, enabling the flow of electric current within the material. As a result, this phenomenon, which is known as optical conductivity, converts solar light into electricity. The relationship between optical conductivity and photon energy is depicted in Fig. 7(e). The initial peaks were positioned at energies of 2.33 eV and 2.38 eV, respectively, for compounds FeTaP and FeTaAs.

The photon absorption coefficients of the FeTaX (X = P, As) HHs are shown in Fig. 7(f). The absorption coefficient was greater than 10^4 cm^{-1} in the visible region, with the maximum absorption at about $13.5 \times 10^5 \text{ cm}^{-1}$ and $14.2 \times 10^5 \text{ cm}^{-1}$ for FeTaX (X = P, As), respectively, as shown in Fig. 7(f). Notably, the absorption spectrum exhibited multiple peaks, which arise

from interband transitions between the bonding and antibonding bands, respectively (Table 3).

Fig. 7(g) depicts the reflectivity $R(\omega)$ versus photon energy curves of FeTaX (X = P, As) HHs. At zero frequency, the reflectivity $R(0)$ was about 39% and 40% for FeTaP and FeTaAs, respectively. In Fig. 7(h), the $L(\omega)$ curves of the FeTaX compounds depict the energy loss experienced by fast electrons as they pass through the material. According to Fig. 7(h), the $L(\omega)$ spectra steadily increase from approximately 1.5 eV until their peak values at around 10 eV. The optical property results advocate the suitability of these materials in optical applications. We have compared our results with those of other experimental works in Table 4.

3.5. Thermoelectric properties

A number of parameters, including the Seebeck coefficient (S), electrical conductivity (σ), and thermal conductivity (κ), influence the performance of a thermoelectric material. Using the Boltzmann semi-classical transport theory, which was implemented in the BoltzTrap code, we computed each of these parameters to determine the thermoelectric response and applicability of the studied compounds. The variation of the Seebeck coefficient of the FeTaX (X = P, As) compounds as a function of temperature is shown in Fig. 8(a), which reveals p-type behavior with a positive Seebeck coefficient magnitude. At room temperature, the computed values of the Seebeck coefficient were found to be $242 \mu\text{V K}^{-1}$, and $240 \mu\text{V K}^{-1}$ for FeTaX (X = P, As) respectively. It was also observed that the values of Seebeck coefficients of FeTaX (X = P, As) decrease as the temperature increases. Due to the intensified random thermal motion and narrow bandgap, which cause the primary charges (such as holes) to jump from the valence band to the conduction band, a phenomenon known as the bipolar effect occurs.⁵³ This causes compensation of carriers and changes in the DOS. The computed outcomes of this study are represented in Table 5 along with the previously available theoretical and experimental results. Our theoretical results are in accordance with those of other experimental works (Table 5). The higher magnitude of S of the studied compounds suggests their applicability in thermoelectric devices.

Electrical conductivity per relaxation time (σ/τ) in relationship with temperature is shown in Fig. 8(b). In contrast to the Coulomb potential, the potential factor shows the energy needed to transfer the charge carriers n and p, demonstrating the electrical conductance of a substance produced by the passage of electrons caused by a temperature differential. We observed that σ/τ increases to reach a maximum of about $2.24 \times 10^{19} (\Omega \text{ mS})^{-1}$ and $2.25 \times 10^{19} (\Omega \text{ mS})^{-1}$ at 900 K for FeTaX (X = P, As) respectively, as represented in Fig. 8(b). However, in Table 5, the values of electrical conductivity at room temperature are reported with other available experimental and theoretical results. The electron and hole velocities, which define the electronic thermal conductivity (κ_e), are related to electrical conductivity by the Wiedemann-Franz law.⁵⁴

As for thermal conductivity (κ/τ), we independently estimated the electronic thermal conductivity (κ_e/τ) and lattice

Table 3 The calculated energy bandgaps (in eV) using different potentials PBE, mBJ and mBJ + SOC

Properties	Other works		
	FeTaP	FeTaAs	Expt ⁶³
PBE	0.882	0.748	1.052
mBJ	0.916	1.002	
mBJ + SOC	0.871	0.993	

Table 4 The calculated optical properties of the FeTaX (for X = P, As) compounds using TB-mBJ potential

Optical properties	Material property	Other works		
		FeTaP	FeTaAs	Expt ⁶⁴
$\varepsilon_1(0)$		19.66	19.96	22.0
$n(0)$		4.43	4.46	
$R(0)$		0.39	0.40	0.75



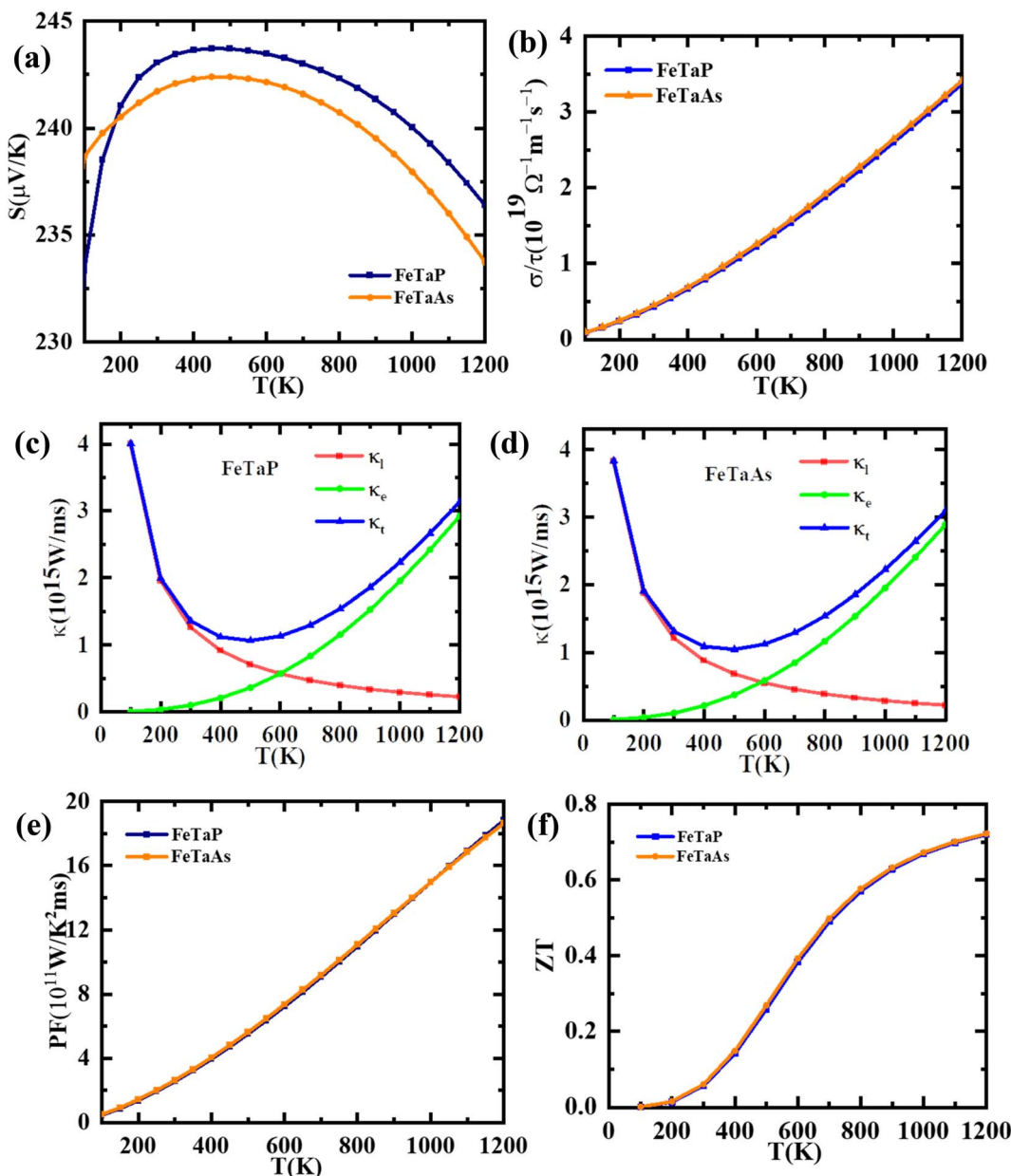


Fig. 8 The computed (a) Seebeck coefficients, (b) electrical conductivity, (c) thermal conductivity, (FeTaP) (d) thermal conductivity (FeTaAs) (e) power factors and (f) figures of merit of FeTaP and FeTaAs as functions of temperature.

Table 5 The calculated transport properties of the FeTaX (for X = P, As) compounds at room temperature using TB-mBJ

Transport properties (300 K)	Material property	FeTaP	FeTaAs	Other works Theory	Other works Expt
	$S (\mu\text{V K}^{-1})$	242	240	235^{60}	$\sim 229^{65}$ $\sim 135^{19}$ 0.41^{19}
	$\sigma/\tau (\Omega\text{ms})^{-1} (10^{19})$	0.49	0.50	0.35^{60}	
	$k_e/\tau (10^{15}) (\text{W m}^{-1} \text{K}^{-1} \text{s}^{-1})$	0.1	0.1		
	$k_l/\tau (10^{15}) (\text{W m}^{-1} \text{K}^{-1} \text{s}^{-1})$	1.20	1.21		4.6^{19}
	$k/\tau (10^{15}) (\text{W m}^{-1} \text{K}^{-1} \text{s}^{-1})$	1.23	1.24		4.8^{19}
	$\text{PF} (10^{10}) (\text{W K}^{-2} \text{m}^{-1} \text{s}^{-1})$	2.1	2.0	0.56^{60}	$\sim 2.8^{65}$ $\sim 1.11^{19}$

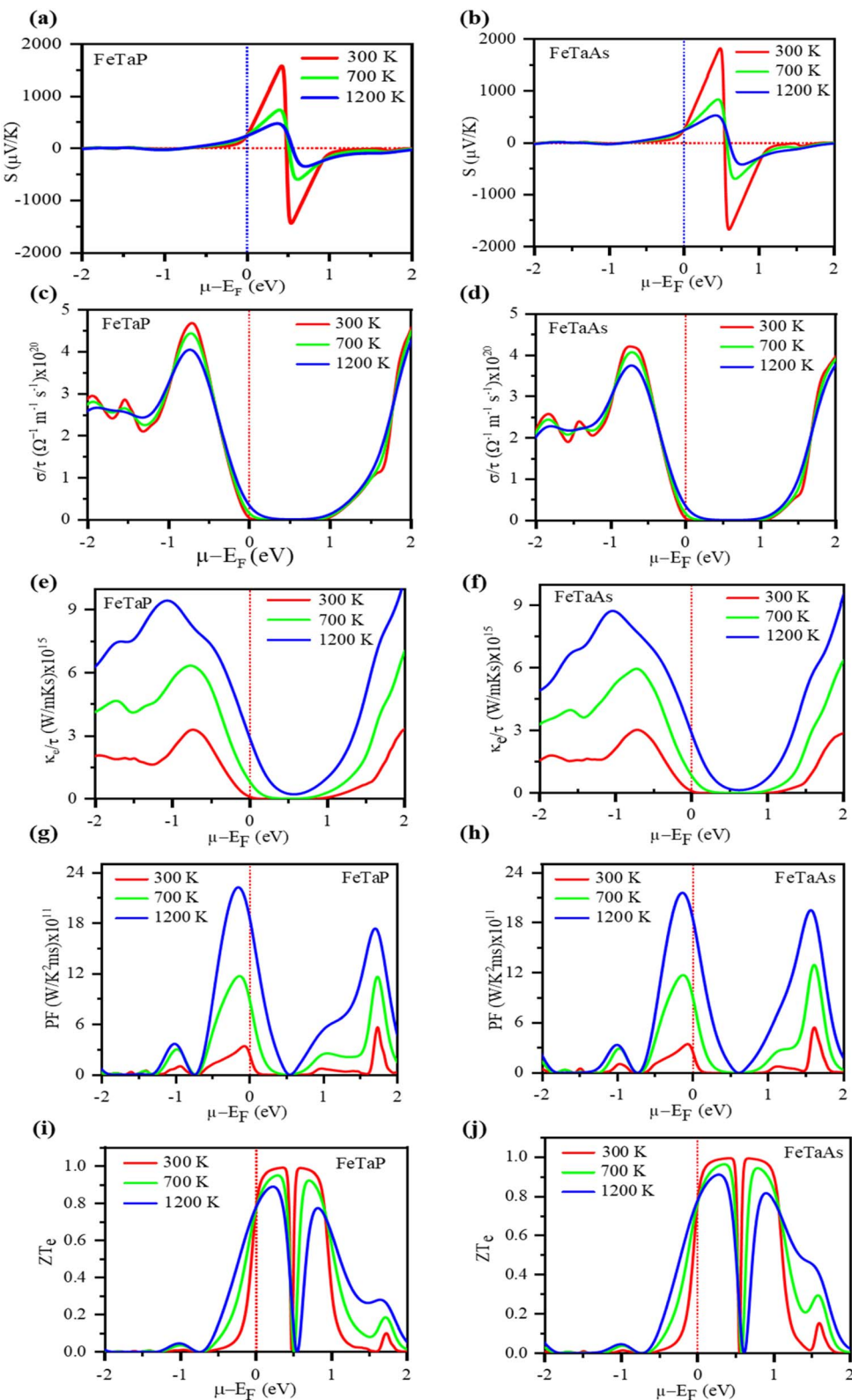


Fig. 9 The computed (a) and (b) Seebeck coefficients, (c) and (d) electrical conductivity, (e) and (f) electrical conductivities, (g) and (h) power factors, and (i) and (j) figures of merit (ZT) of FeTaP and FeTaAs as functions of chemical potential, respectively.

thermal conductivity (κ_l/τ) of the materials under consideration. Moreover, the BoltzTrap code was utilised to estimate κ_e/τ , and the Slack equation^{55,56} was applied to estimate κ_l/τ during the calculation process:

$$\kappa = \frac{A \bar{M} \theta_D^3 V^{1/3}}{\gamma^2 T n^{2/3}} \quad (17)$$

where M is the average atomic mass, θ_D is the Debye temperature, V is the volume per atom, n is the number of atoms per unit cell, γ is the Gruneisen parameter and A is defined as follows:

$$A = \frac{2.43 \times 10^{-8}}{1 - \frac{0.514}{\gamma} + \frac{0.228}{\gamma^2}} \quad (18)$$

Therefore, κ/τ is a combination of κ_e/τ and κ_l/τ calculated as $\kappa = \kappa_e + \kappa_l$. In Fig. 8(c) and (d), we have plotted the individual and combined variation in thermal conductivity of FeTaP and FeTaAs HHs with temperature, respectively. The highest contribution of κ_e/τ to the overall thermal conductivity of both compounds can be clearly seen in the figure in comparison with κ_l/τ . The decrease in κ_l/τ is caused by an increase in phonon scattering, which happens when temperature increases. κ_e/τ substantially rises with temperature and reaches the maximum at a high temperature, demonstrating the same trend as the electrical conductivity. The calculated values at room temperature are summarized in Table 5 and compared with the available experimental and theoretical reports. Fig. 8(e) displays the power factor (eqn (6)) as a function of temperature. The PF of both compounds is strongly influenced by the change in temperature. The calculated values of PF at room temperature are given in Table 5. These results are compared with the other materials.

Fig. 8(f) illustrates the temperature-dependent behavior of the thermoelectric figure of merit (ZT) of the FeTaX materials. The data reveals that as the temperature rises, the ZT of FeTaP increases, reaching a peak value of approximately 0.71 at 1200 K. In contrast, FeTaAs achieves a maximum value of about 0.72 at 1200 K. These findings indicate the potential suitability of the FeTaX materials for use in thermoelectric devices.

Fig. 9(a) and (b) depict the Seebeck coefficient (S) as a function of the chemical potential (μ). Along the chemical potential axis, the doping range of a material is shown as positive for n-type and negative for p-type. Fig. 9(a) and (b) demonstrate that the Seebeck coefficients decrease with temperature.⁵⁷ The maximum Seebeck coefficient was determined to be 1681 $\mu\text{V K}^{-1}$ for FeTaP at 300 K and 0.5 eV and 1825 for FeTaAs. Fig. 9(c) and (d) show the electrical conductivity per relaxation time (τ) of the two compounds in the chemical potential range of -2.0 eV to 2.0 eV at various temperatures, such as 300 K, 700 K, and 1200 K. In the chemical range of 0.0 eV to 1.0 eV, the value was found to be zero. Thereafter, it starts to increase with both sides of the chemical potential, exhibiting opposite behaviour above 1.48 eV for FeTaP in the investigated chemical potential range. FeTaAs also follows a similar trend. FeTaP is observed to exhibit the reverse behaviour of decreasing with temperature above 0.6 eV when the same trend is followed for that material. The highest value of electrical

conductivity was discovered to be for p-type in both compounds, that is, on the negative side of the chemical potential axis. In Fig. 8(e) and (f), the fluctuations of electronic thermal conductivity with chemical potential are presented. The value is 0 at chemical potentials between 0.3 and 0.7 eV. From 300 K to 1200 K, the electronic thermal conductivity of both compounds increases with temperature. As shown in Fig. 9(g) and (h), the dependency of power factor (PF) on the chemical potential was explored for both compounds in the chemical potential range of -2.0 eV to 2.0 eV at 300 K, 700 K, and 1200 K, respectively. While FeTaP revealed an ideal power factor value of -0.2 eV, FeTaAs had a peak value of -0.2 eV. At different temperatures (300 K, 700 K, and 1200 K), the fluctuation of the figure of merit with the chemical potential was investigated in the chemical potential range of -2.0 eV to 2.0 eV, and the results are shown in Fig. 9(i) and (j).⁵⁸ As demonstrated in Fig. 9(i), for both compounds, the figure of merit is close to the Fermi level at ambient temperature and reaches the ideal value of roughly unity at 0.3 eV. In the range of 0 eV to 1.3 eV in the n-type region, it decreases with temperature in the cases of FeTaP and FeTaAs, but in the p-type region, it increases with temperature.⁵⁹ The high figures of merit exhibited by the compounds in a suitable chemical potential range indicate that they are possible candidates for thermoelectric applications.

4. Conclusion

In this investigation, we employed the FP-LAPW method to perform *ab initio* computations, focusing on the structural, optical, and thermoelectric characteristics of cubic FeTaX (X = P, As) compounds. To determine the structural ground state, we utilized PBE-GGA exchange correlations. The TB-mBJ approach was considered for the estimation of the electronic properties of the investigated FeTaX (X = P, As) compounds. The calculated lattice constants, bulk modulus, and other ground-state characteristics are in good accordance with other theoretical findings. The cubic FeTaX (X = P, As) compounds exhibit semiconducting properties, as per the estimated electronic properties. Their optical spectra were calculated in the energy range of 0–10 eV, and the optical characteristics were analyzed. The study shows that FeTaX (X = P, As) are optically active. However, the investigated materials exhibit low values of ZT at room temperature (0.71 and 0.72 at 1200 K for FeTaP and FeTaAs, respectively). The compounds can be used in thermoelectric devices due to their high figures of merit at high temperatures. Further, under suitable chemical potentials, these materials may exhibit high values of ZT even at room temperature.

Data availability

The raw/processed data can be made available with a reasonable request to the corresponding author.

Conflicts of interest

The authors declare that they have no known competing financial interests or personal relationships that could have appeared to influence the work reported in this paper.



Acknowledgements

This research was funded by the Princess Nourah bint Abdulrahman University Researchers Supporting Project number (PNURSP2024R7), Princess Nourah bint Abdulrahman University, Riyadh, Saudi Arabia. The authors extend their appreciation to the Deanship of Scientific Research at King Khalid University for funding this work through research groups program under grant number (RGP.2/586/44).

References

- 1 M. H. Elsheikh, D. A. Shnawah, M. F. M. Sabri, S. B. M. Said, M. H. Hassan, M. B. A. Bashir and M. Mohamad, A Review on Thermoelectric Renewable Energy: Principle Parameters That Affect Their Performance, *Renewable Sustainable Energy Rev.*, 2014, **30**, 337–355.
- 2 J. A. Abraham, D. Behera, K. Kumari, A. Srivastava, R. Sharma and S. K. Mukherjee, A Comprehensive DFT Analysis on Structural, Electronic, Optical, Thermoelectric, SLME Properties of New Double Perovskite Oxide Pb_2ScBiO_6 , *Chem. Phys. Lett.*, 2022, 139987.
- 3 J. Twidell, *Renewable Energy Resources*, Routledge, 2021, ISBN 0429452160.
- 4 N. Mingo, Thermoelectric Fig. of Merit and Maximum Power Factor in III–V Semiconductor Nanowires, *Appl. Phys. Lett.*, 2004, **84**, 2652–2654.
- 5 D. Nemir and J. Beck, On the Significance of the Thermoelectric Fig. of Merit Z, *J. Electron. Mater.*, 2010, **39**, 1897–1901.
- 6 Z. Liu, S. Guo, Y. Wu, J. Mao, Q. Zhu, H. Zhu, Y. Pei, J. Sui, Y. Zhang and Z. Ren, Design of High-performance Disordered Half-Heusler Thermoelectric Materials Using 18-electron Rule, *Adv. Funct. Mater.*, 2019, **29**, 1905044.
- 7 J. A. Abraham, R. Sharma, S. Ahmad and A. Dey, DFT Investigation on the Electronic, Optical and Thermoelectric Properties of Novel Half-Heusler Compounds $ScAuX$ ($X = Si, Ge, Sn, Pb$) for Energy Harvesting Technologies, *Eur. Phys. J. Plus*, 2021, **136**, 1091.
- 8 D. Behera, A. Azzouz-Rached, A. Bouhenna, M. M. Salah, A. Shaker and S. K. Mukherjee, First-Principles Studies on the Physical Properties of the Half Heusler $RbNbCd$ and $RbNbZn$ Compounds: A Promising Material for Thermoelectric Applications, *Crystals*, 2023, **13**, 618.
- 9 T. Gruhn, Comparative Ab Initio Study of Half-Heusler Compounds for Optoelectronic Applications, *Phys. Rev. B*, 2010, **82**, 125210.
- 10 S. Kacimi, H. Mehnane and A. Zaoui, I–II–V and I–III–IV Half-Heusler Compounds for Optoelectronic Applications: Comparative Ab Initio Study, *J. Alloys Compd.*, 2014, **587**, 451–458.
- 11 Y. O. Ciftci and S. D. Mahanti, Electronic Structure and Thermoelectric Properties of Half-Heusler Compounds with Eight Electron Valence Count— $KScX$ ($X = C$ and Ge), *J. Appl. Phys.*, 2016, **119**, 145703.
- 12 K. Ciesielski, K. Synoradzki, I. Wolańska, P. Stachowiak, L. Kępiński, A. Jeżowski, T. Toliński and D. Kaczorowski, High-Temperature Power Factor of Half-Heusler Phases $RENiSb$ ($RE = Sc, Dy, Ho, Er, Tm, Lu$), *J. Alloys Compd.*, 2020, **816**, 152596.
- 13 M. J. Winiarski, K. Bilińska, K. Ciesielski and D. Kaczorowski, Thermoelectric Performance of P-Type Half-Heusler Alloys $ScMSb$ ($M = Ni, Pd, Pt$) by Ab Initio Calculations, *J. Alloys Compd.*, 2018, **762**, 901–905.
- 14 Y. Pan, A. M. Nikitin, T. V. Bay, Y. K. Huang, C. Paulsen, B. H. Yan and A. De Visser, Superconductivity and Magnetic Order in the Noncentrosymmetric Half-Heusler Compound $ErPdBi$, *Europhys. Lett.*, 2013, **104**, 27001.
- 15 S. Populoh, M. H. Aguirre, O. C. Brunko, K. Galazka, Y. Lu and A. Weidenkaff, High Fig. of Merit in (Ti, Zr, Hf) $NiSn$ Half-Heusler Alloys, *Scr. Mater.*, 2012, **66**, 1073–1076.
- 16 C. Fu, S. Bai, Y. Liu, Y. Tang, L. Chen, X. Zhao and T. Zhu, Realizing High Fig. of Merit in Heavy-Band p-Type Half-Heusler Thermoelectric Materials, *Nat. Commun.*, 2015, **6**, 8144.
- 17 J.-W. G. Bos, Recent Developments in Half-Heusler Thermoelectric Materials, *Thermoelectr. Energy Convers.*, 2021, 125–142.
- 18 D. Behera, J. A. Abraham, R. Sharma, S. K. Mukherjee and E. Jain, First Principles Study of New D0 Half-Metallic Ferromagnetism in $CsBaC$ Ternary Half-Heusler Alloy, *J. Supercond. Novel Magn.*, 2022, **35**, 3431–3437.
- 19 Q. Wang, X. Xie, S. Li, Z. Zhang, X. Li, H. Yao, C. Chen, F. Cao, J. Sui, X. Liu and Q. Zhang, Enhanced thermoelectric performance in $Ti(Fe, Co, Ni)Sb$ pseudo-ternary half-Heusler alloys, *J. Materomics*, 2021, **7**(4), 756–765.
- 20 H. Zhu, J. Mao, Y. Li, J. Sun, Y. Wang, Q. Zhu, G. Li, Q. Song, J. Zhou, Y. Fu and R. He, Discovery of $TaFeSb$ -based half-Heuslers with high thermoelectric performance, *Nat. Commun.*, 2019, **10**(1), 270.
- 21 S. Zahir, N. Mehmood, R. Ahmad, S. Khan, A. U. Rahman and A. Dahshan, Structural, elastic, mechanical, electronic, magnetic and optical properties of half-Heusler compounds $CoFeZ$ ($Z = P, As, Sb$): A GGA+ U approximation, *Mater. Sci. Semicond. Process.*, 2022, **143**, 106445.
- 22 D. Koller, F. Tran and P. Blaha, Merits and Limits of the Modified Becke-Johnson Exchange Potential, *Phys. Rev. B*, 2011, **83**, 195134.
- 23 P. Blaha, K. Schwarz, G. K. H. Madsen, D. Kvasnicka and J. Luitz, *Wien2k. An augmented plane wave+ local orbitals program for calculating crystal properties*, 2001, vol. 60.
- 24 C. Ambrosch-Draxl and J. O. Sofo, Linear Optical Properties of Solids within the Full-Potential Linearized Augmented Planewave Method, *Comput. Phys. Commun.*, 2006, **175**, 1–14.
- 25 J. P. Perdew, K. Burke and M. Ernzerhof, Generalized Gradient Approximation Made Simple, *Phys. Rev. Lett.*, 1996, **77**, 3865.
- 26 D. Behera, R. Sharma, H. Ullah, H. S. Waheed and S. K. Mukherjee, Electronic, Optical, and Thermoelectric Investigations of Zintl Phase AAg_2Se_2 ($A = Sr, Ba$) Compounds: A First Principles Approach, *J. Solid State Chem.*, 2022, 123259.



27 M. Jamal, M. Bilal, I. Ahmad and S. Jalali-Asadabadi, IRelast Package, *J. Alloys Compd.*, 2018, **735**, 569–579.

28 H. Ehrenreich and M. H. Cohen, Self-consistent field approach to the many-electron problem, *Phys. Rev.*, 1959, **115**(4), 786.

29 J. Sun, H.-T. Wang, J. He and Y. Tian, Ab initio investigations of optical properties of the high-pressure phases of ZnO, *Phys. Rev. B*, 2005, **71**(12), 125132.

30 G. K. H. Madsen and D. J. Singh, BoltzTraP. A Code for Calculating Band-Structure Dependent Quantities, *Comput. Phys. Commun.*, 2006, **175**, 67–71.

31 T. Katsura and Y. Tange, A Simple Derivation of the Birch–Murnaghan Equations of State (EOSs) and Comparison with EOSs Derived from Other Definitions of Finite Strain, *Minerals*, 2019, **9**, 745.

32 D. Behera and S. K. Mukherjee, Theoretical Investigation of the Lead-Free K2InBiX6 (X= Cl, Br) Double Perovskite Compounds Using First Principle Calculation, *JETP Lett.*, 2022, **1**–10.

33 D. Behera, B. Mohammed, S. Taieb, B. Mokhtar, S. Al-Qaisi and S. K. Mukherjee, First-Principle Investigations on Optoelectronics and Thermoelectric Properties of Lead-Free Rb2InSbX6 (X= Cl, Br) Double Perovskites: For Renewable Energy Applications, *Eur. Phys. J. Plus*, 2023, **138**, 520.

34 O. M. Abid, S. Menouer, A. Yakoubi, H. Khachai, S. B. Omran, G. Murtaza, D. Prakash, R. Khenata and K. D. Verma, Structural, Electronic, Elastic, Thermoelectric and Thermodynamic Properties of the NbMSb Half Heusler (M= Fe, Ru, Os) Compounds with First Principle Calculations, *Superlattices Microstruct.*, 2016, **93**, 171–185.

35 Born, M. K. Huang, *Dynamical Theory of Crystal Lattices*. Oxford University Press, 1954.

36 I. Waller, Dynamical Theory of Crystal Lattices by M. Born and K. Huang, *Acta Crystallogr.*, 1956, **9**, 837–838.

37 S. Lakra and S. Kumar Mukherjee, Study of Structural, Electronic, Optical and Thermodynamic Properties of SnSiO₃ Compound: A DFT Study, *Mater. Today: Proc.*, 2023, DOI: [10.1016/j.matpr.2023.01.231](https://doi.org/10.1016/j.matpr.2023.01.231).

38 S. F. Pugh, XCII. Relations between the Elastic Moduli and the Plastic Properties of Polycrystalline Pure Metals, *Lond. Edinb. Dublin philos. mag. j. sci.*, 1954, **45**, 823–843.

39 S. F. Pugh, *Lond. Edinb. Dublin philos. mag. j. sci.*, 1954, **45**, 823.

40 I. N. Frantsevich, *Elastic Constants and Elastic Moduli of Metals and Insulators. Reference book*, 1982.

41 M. E. Eberhart and T. E. Jones, Cauchy Pressure and the Generalized Bonding Model for Nonmagnetic Bcc Transition Metals, *Phys. Rev. B*, 2012, **86**, 134106.

42 C. M. Kube, Elastic Anisotropy of Crystals, *AIP Adv.*, 2016, **6**, 95209.

43 S. Al-Qaisi, H. Rached, T. A. Alrebd, S. Bouzgarrou, D. Behera, S. K. Mukherjee, M. Khuili, M. Adam, A. S. Verma and M. Ezzeldien, Study of Mechanical, Optical, and Thermoelectric Characteristics of Ba₂XM₀6 (X= Zn, Cd) Double Perovskite for Energy Harvesting, *J. Comput. Chem.*, 2023, **44**, 2442–2452.

44 S. A. Dar, V. Srivastava, U. K. Sakalle, V. Parey and G. Pagare, DFT investigation on electronic, magnetic, mechanical and thermodynamic properties under pressure of some EuMO₃ (M= Ga, In) perovskites, *Mater. Res. Express*, 2017, **4**(10), 106104.

45 M. K. Y. Chan and G. Ceder, Efficient Band Gap Prediction for Solids, *Phys. Rev. Lett.*, 2010, **105**, 196403.

46 D. Behera, M. Manzoor, M. W. Iqbal, S. Lakra and S. K. Mukherjee, Revealing Excellent Electronic, Optical, and Thermoelectric Behavior of EU Based EuAg₂Y₂ (Y = S/ Se): for Solar Cell Applications, *Comput. Condens. Matter*, 2022, **32**, e00723.

47 X. Ma, Y. Wu, Y. Lv and Y. Zhu, Correlation Effects on Lattice Relaxation and Electronic Structure of ZnO within the GGA+U Formalism, *J. Phys. Chem. C*, 2013, **117**, 26029–26039, DOI: [10.1021/jp407281x](https://doi.org/10.1021/jp407281x).

48 D. Behera and S. K. Mukherjee, First-Principles Calculations to Investigate Structural, Optoelectronics and Thermoelectric Properties of Lead Free Cs₂GeSnX₆ (X= Cl, Br), *Mater. Sci. Eng. B*, 2023, **292**, 116421.

49 O. Rubel, F. Tran, X. Rocquefelte and P. Blaha, Perturbation Approach to Ab Initio Effective Mass Calculations, *Comput. Phys. Commun.*, 2021, **261**, 107648.

50 L. Hnamte, H. Joshi and R. K. Thapa, Electronic and Optical Properties of Double Perovskite Oxide Pb 2 ScSbO 6: A First Principles Approach, *IOSR J. Appl. Phys.*, 2018, **10**, 39–44.

51 D. Behera, A. Dixit, B. Nahak, A. Srivastava, R. Sharma, R. Khenata, S. Bin-Omran, S. A. M. Abdelmohsen, A. M. M. Abdelbacki and S. K. Mukherjee, Theoretical Insight on the Electronic Band Structure, Mechanical, Vibrational and Thermodynamic Characteristic of Antiperovskites RE₃InN (RE= Y and La), *Mater. Today Commun.*, 2023, **35**, 105618.

52 D. Behera, M. Manzoor, M. Maharana, M. W. Iqbal, T. Zahid, S. Lakra, S. K. Mukherjee and S. S. Alarfaji, Structural, Electronic, Optical, and Thermoelectric Response of Zintl Phase AAg₂S₂ (A= Sr/Ba) Compounds for Renewable Energy Applications, *Phys. B*, 2023, **649**, 414446.

53 V. Ponnambalam, S. Lindsey, W. Xie, D. Thompson, F. Drymiotis and T. M. Tritt, High Seebeck Coefficient AMXP₂ (A= Ca and Yb; M, X= Zn, Cu and Mn) Zintl Phosphides as High-Temperature Thermoelectric Materials, *J. Phys. D: Appl. Phys.*, 2011, **44**, 155406.

54 M. Jonson and G. D. Mahan, Mott's Formula for the Thermopower and the Wiedemann-Franz Law, *Phys. Rev. B*, 1980, **21**, 4223.

55 G. A. Slack, in *Solid State Physics: Advances in Research and Applications*, ed. H. Ehrenreich, F. Seitz, and D. Turnbull, Academic Press, New York, 1979, vol. 34, p. 1.

56 G. A. Slack, Nonmetallic crystals with high thermal conductivity, *J. Phys. Chem. Solids*, 1973, **34**(2), 321–335.

57 A. Saxena, A. Dixit, D. Behera, J. A. Abraham, R. Sharma and S. K. Mukherjee, Insight on Structural, Electronic and Thermoelectric Properties of Perovskite AgBaCl₃ by an Ab-Initio for Solar Cell and Renewable Energy, *Mater. Today: Proc.*, 2023.



58 N. Wang, C. Shen, Z. Sun, H. Xiao, H. Zhang, Z. Yin and L. Qiao, High-Temperature Thermoelectric Monolayer Bi₂TeSe₂ with High Power Factor and Ultralow Thermal Conductivity, *ACS Appl. Energy Mater.*, 2022, **5**, 2564–2572.

59 V. F. Kharlamov, Thermoelectric Fig. of Merit of a Material Consisting of Semiconductor or Metal Particles, *J. Exp. Theor. Phys.*, 2013, **117**, 83–88.

60 D. Behera and S. K. Mukherjee, Insight to Structural, Electronic, Optical and Thermoelectric Properties of NaCaSb and KCaSb Half Heusler Compounds: A DFT Approach, *JETP Lett.*, 2023, 1–14.

61 A. K. Verma, K. K. Johari, K. Tyagi, D. K. Sharma, P. Kumar, S. Kumar, S. Bathula, S. R. Dhakate and B. Gahtori, Role of sintering temperature on electronic and mechanical properties of thermoelectric material: A theoretical and experimental study of TiCoSb half-Heusler alloy, *Mater. Chem. Phys.*, 2022, **281**, 125854.

62 G. Rogl, A. Grytsiv, M. Gürth, A. Tavassoli, C. Ebner, A. Wünschek, S. Puchegger, V. Soprunguk, W. Schranz, E. Bauer, H. Müller, M. Zehetbauer and P. Rogl, Mechanical properties of half-Heusler alloys, *Acta Mater.*, 2016, **107**, 178–195.

63 S. Kacimi, H. Mehnane and A. Zaoui, I-II-V and I-III-IV half-Heusler compounds for optoelectronic applications: Comparative ab initio study, *J. Alloys Compd.*, 2014, **587**, 451–458.

64 S. Ouardi, G. H. Fecher, C. Felser, J. Hamrle, K. Postava and J. Pištora, Transport and optical properties of the gapless Heusler compound PtYSb, *Appl. Phys. Lett.*, 2011, **99**, 211904.

65 I. Ioannou, S. P. Ioannou, A. Delimitis, Y. Gelbstein, I. Giapintzakis and T. Kyratsi, High thermoelectric performance of p-type half-Heusler (Hf,Ti)Co(Sb,Sn) solid solutions fabricated by mechanical alloying, *J. Alloys Compd.*, 2021, **858**, 158330.

